First evaluation of the climatological calibration algorithm in the real-time TMPA precipitation estimates over two basins at high and low latitudes

Bin Yong,[1,2] Liliang Ren,[1] Yang Hong,[2] Jonathan J. Gourley,[3] Yudong Tian,[4,5] George J. Huffman,[6] Xi Chen,[1] Weiguang Wang,[1] and Yixin Wen[2]

Received 18 September 2012; revised 9 April 2013; accepted 10 April 2013; published 17 May 2013.

[1] The TRMM Multi-satellite Precipitation Analysis (TMPA) system underwent a crucial upgrade in early 2009 to include a climatological calibration algorithm (CCA) to its real-time product 3B42RT, and this algorithm will continue to be applied in the future Global Precipitation Measurement era constellation precipitation products. In this study, efforts are focused on the comparison and validation of the Version 6 3B42RT estimates before and after the climatological calibration is applied. The evaluation is accomplished using independent rain gauge networks located within the high-latitude Laohahe basin and the low-latitude Mishui basin, both in China. The analyses indicate the CCA can effectively reduce the systematic errors over the low-latitude Mishui basin but misrepresent the intensity distribution pattern of medium-high rain rates. This behavior could adversely affect TMPA's hydrological applications, especially for extreme events (e.g., floods and landslides). Results also show that the CCA tends to perform slightly worse, in particular, during summer and winter, over the high-latitude Laohahe basin. This is possibly due to the simplified calibration-processing scheme in the CCA that directly applies the climatological calibrators developed within 40° latitude to the latitude belts of 40°N–50°N. Caution should therefore be exercised when using the calibrated 3B42RT for heavy rainfall-related flood forecasting (or landslide warning) over high-latitude regions, as the employment of the smooth-fill scheme in the CCA bias correction could homogenize the varying rainstorm characteristics. Finally, this study highlights that accurate detection and estimation of snow at high latitudes is still a challenging task for the future development of satellite precipitation retrievals.

Citation: Yong, B., L. Ren, Y. Hong, J. J. Gourley, Y. Tian, G. J. Huffman, X. Chen, W. Wang, and Y. Wen (2013), First evaluation of the climatological calibration algorithm in the real-time TMPA precipitation estimates over two basins at high and low latitudes, *Water Resour. Res.*, *49*, 2461–2472, doi:10.1002/wrcr.20246.

1. Introduction

[2] The upcoming Global Precipitation Measurement (GPM) mission, with an approaching launch date of early 2014 (http://pmm.nasa.gov/GPM), will employ an international constellation of microwave sensors. It is anticipated that GPM will provide more accurate global rainfall products at higher spatial and temporal resolution (0.1°, 1 h), improving our scientific understanding of Earth's water and energy cycle and extending current observational capabilities for extreme weather events that cause natural hazards and disasters [*Tian et al.*, 2007; *Kidd and Huffman*, 2011; *Tapiador et al.*, 2012]. The current operational Tropical Rainfall Measuring Mission (TRMM) Multi-satellite Precipitation Analysis (TMPA) system is intended to produce the best estimates of quasi-global precipitation from almost all available satellite-borne precipitation-related sensors by applying calibration by TRMM sensor products [*Huffman et al.*, 2007]. In particular, the TMPA real-time product 3B42RT, which combines the high-quality passive microwave (HQ; 3B40RT) and microwave-calibrated geostationary infrared (VAR; 3B41RT), provides three hourly, 0.25° × 0.25° latitude/longitude gridded precipitation data for the latitude band 50°N–50°S [*Huffman et al.*, 2010]. It is the near-real-time availability (6–9 h latency) and relatively

[1]State Key Laboratory of Hydrology-Water Resources and Hydraulic Engineering, Hohai University, Nanjing, China.
[2]School of Civil Engineering and Environmental Sciences, University of Oklahoma, Norman, Oklahoma, USA.
[3]Office of Oceanic and Atmospheric Research, NOAA/National Severe Storms Laboratory, Norman, Oklahoma, USA.
[4]Earth System Science Interdisciplinary Center, University of Maryland, College Park, Maryland, USA.
[5]Hydrological Sciences Branch, NASA Goddard Space Flight Center, Greenbelt, Maryland, USA.
[6]Science Systems and Applications, Inc., and Laboratory for Atmospheres, NASA Goddard Space Flight Center, Greenbelt, Maryland, USA.

Corresponding author: B. Yong, State Key Laboratory of Hydrology-Water Resources and Hydraulic Engineering, Hohai University, Nanjing 210098, China. (yongbin_hhu@126.com)

©2013. American Geophysical Union. All Rights Reserved.
0043-1397/13/10.1002/wrcr.20246

fine resolution that make 3B42RT attractive for a variety of hydrological applications and natural hazard warning, such as flood monitoring and landslide detection at local, regional, and even global scale [e.g., *Hossain and Lettenmaier*, 2006; *Hong et al*., 2007].

[3] As new sensors and algorithms have been integrated, the TMPA real-time system has undergone several upgrades for improving the data accuracy and algorithm stability during the past decade. (A detailed description regarding the dynamic evolution of the 3B42RT algorithm is provided in Appendix A of *Yong et al*. [2012].) In Version 6 of the TMPA real-time system (hereafter "3B42RT-Version 6"), there was an important algorithmic upgrade, i.e., climatological calibration algorithm (CCA), which occurred on 17 February 2009. For this new calibration procedure, the developers first determined a local histogram matching of three hourly 2A12 (TRMM Microwave Imager (TMI)) to 2B31 (TRMM Combined Instrument (TCI)), computed from 10 years of coincident data to establish the climatology for each calendar month. Then, a monthly climatological calibration of TCI to 3B43V6 (another TRMM product that combines the merged HQ/VAR estimates and the monthly accumulated Climate Assessment and Monitoring System (CAMS) [*Xie and Arkin*, 1996] precipitation gauge analyses during the period of interest with an approach of inverse random error variance weighting at monthly time intervals) is computed as a simple ratio on a $1^\circ \times 1^\circ$ grid. The calibration factor is aggregated to an overlapping $3^\circ \times 3^\circ$ template using 10 years of data. Finally, the TMI-TCI and TCI-3B43 calibrations are successively applied to the preliminary real-time products to create the calibrated 3B42RT estimates. Though this climatological bias correction indirectly uses the precipitation gauge data (i.e., CAMS in Version 6) to rescale the purely satellite-derived HQ/VAR estimates, these adjustments are based on the climatological monthly data. Thus, this makes 3B42RT independent of the month-to-month ground gauge observations used in the TMPA postreal-time product 3B42V6.

[4] The CCA is the primary upgrade from the original 3B42RT-Version 5 to Version 6. Furthermore, this new calibration has been undergoing tests in the new Version 7 real-time system. The new, real-time Version 7 of TRMM product 3B42 (the replacement for Version 6) is quite valuable to a number of users and applications due to the increased latency of the post-real-time data sets (about 2 months after the end of the month in 3B42V7 versus 10 days after the month for 3B42V6). The same CCA approach has just been used in testing Version 7 (see ftp://trmmopen.gsfc.nasa.gov/pub/merged/V7Documents/3B4XRT_doc_V7.pdf; note: Version 7 employs the Global Precipitation Climatology Center (GPCC) [*Rudolf et al*., 1994] monthly data set as the gauge analysis in CCA), and a similar approach is envisioned for the real-time runs of the day-1 multisatellite algorithm in GPM. Therefore, it seems timely for this paper to employ independent surface gauge observations to directly compare and validate the CCA algorithm and offer some insights for future development.

[5] In this paper, the "new" climatologically calibrated precipitation estimates and the original uncalibrated combined precipitation estimates from 3B42RT-Version 6 are statistically investigated over two basins in China at different latitudes with independent gauge observation networks. Our aim is to first compare the differences between uncalibrated and calibrated precipitation fields and validate whether the TMPA real-time estimates have been significantly improved after the climatological calibration. By further analyzing their performance for two distinct basins, we also attempted to detect the limitations of this new calibration, which is of great interest to both the retrieval developers and the data users.

2. Study Basins and Data Sources

[6] The two basins in China we studied are the high-latitude Laohahe basin, situated beyond the TRMM TMI/precipitation radar (PR) nominal coverage (38°N-S), and the low-latitude Mishui basin, located within the TRMM nominal coverage, respectively (Figure 1). The Laohahe basin, with a drainage area of 18,112 km^2, lies upstream of the West Liao River at latitude of 41°N–42.75°N and longitude of 117.25°E–120°E. The basin elevation ranges from 2017 m in the upstream mountainous area to 427 m above sea level at the channel outlet of the Xinglongpo hydrological station, with the topography significantly descending from west to east. The climate of this basin is that of a typical semiarid region, with its average annual precipitation, runoff, and air temperature during the past half century (1956–2010) being 418.3 mm, 28.7 mm, and 7.5°C, respectively [*Yong et al*., 2013]. Similar to other semiarid basins, the annual potential evaporation of the Laohahe basin exceeds annual precipitation. Summer is the main rainy season with about 50%–60% of the annual precipitation occurring in June, July, and August. Compared to other basins in the northern part of China, this basin has an extraordinarily dense observation network of 52 conventional rain gauges that can provide reliable ground verification for the satellite precipitation estimates. The Mishui basin is located within 26°N–27.5°N and 113°E–114.25°E at the junction of Hunan and Jiangxi Provinces in the southeast of China with a subtropical humid climate. The basin has complex topography with elevations ranging from 49 m at the northwest outlet (i.e., Ganxi hydrological station) to 2093 m at the highest peak of southeast mountains. Altogether, there are 35 rain gauges evenly distributed within this 10,305 km^2 basin. The average annual precipitation, runoff, and air temperature are approximately 1561.2 mm, 985.2 mm, and 18.0°C, respectively [*Jiang et al*., 2012]. The hydrological regime of this basin has a distinct seasonal pattern. Approximately 65% of the total annual precipitation occurs between April and September. Particularly in the rainy summer months (June-August), basinwide storms with high-intensity and long-duration rainfall frequently result in floods and associated landslides. For example, the heavy rainstorms in 2004 induced 64 flash floods, approximately 2300 landslides, and more than 130 debris flows, which directly caused 54 of deaths and 54.76 billion of Chinese Yuan in damages [*Liang and Liu*, 2010].

[7] The rain gauge networks in these two basins are both maintained by the Chinese Ministry of Water Resources. The Chinese rain gauge data in GPCC and CAMS are collected from the national standard stations operated by the China Meteorological Administration (CMA), so the ground observations in this study are independent from what *Huffman et al*. [2010] used for 3B42RT-Version 6 CCA. Moreover, the quality of observed data is double

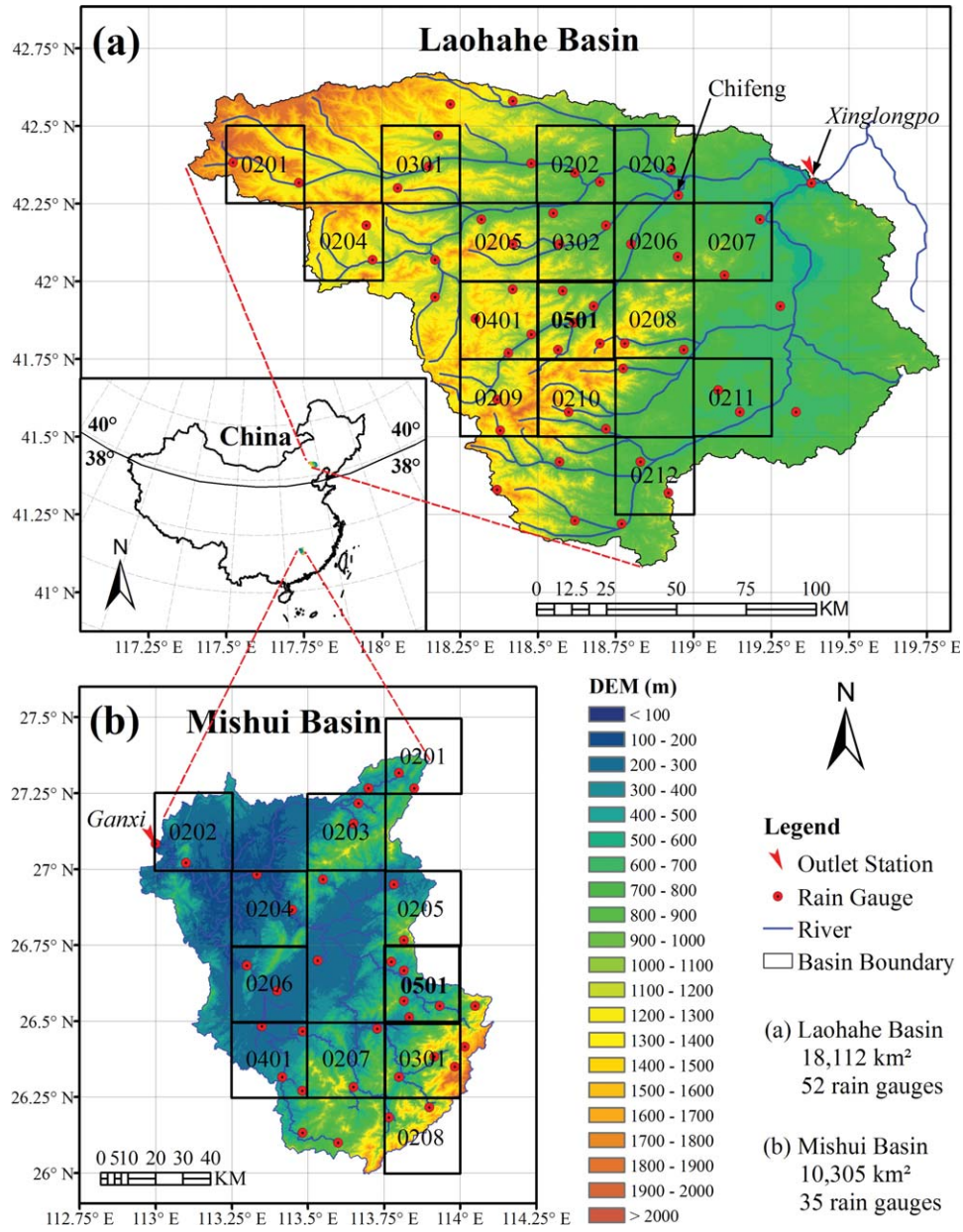

Figure 1. Map of the (a) Laohahe and (b) Mishui basins, rain gauge distributions, and sampling strategies used in this study. The curved line on the inset map denotes the northern edge of TRMM data coverage. Black squares represent the 16 selected 0.25° × 0.25° grid boxes in Laohahe basin and the 11 grid boxes in Mishui basin for verification of satellite precipitation estimates. Numbers are grid IDs (e.g., 0501 indicates the first grid box containing five gauge stations, and 0202 represents the second grid box containing two gauges).

checked under strict guidelines, which are detailed by *Yong et al*. [2010, 2012]. To reduce the scale errors caused by the direct comparison between the gridded satellite estimates and the point-scale gauge data, we only selected grid boxes that contained at least two gauges and then used the average value of all gauges within one grid as the ground truth, as adopted by some previous studies [*Adler et al*., 2003; *Chokngamwong and Chiu*, 2008; *Yong et al*., 2010]. Following this sampling strategy, 16 0.25° × 0.25° grid boxes corresponding to TRMM pixel resolution were picked out for the Laohahe basin, and 11 grid boxes were selected for the Mishui basin (Figure 1).

[8] Some recent studies have reported on the changes of the relative accuracy and the hydrologic performance of 3B42RT estimates over its different evolving periods [e.g., *Su et al*., 2011; *Yong et al*., 2012]. However, it is worthwhile to point out that these evaluations across the time history of various algorithmic phases mix potential effects due to the varying storm or snowfall characteristics during various years and the changes in the retrieval algorithms themselves. In this study, therefore, we adopted an approach for directly comparing the uncalibrated and calibrated 3B42RT estimates (hereafter referred to as "3B42RT-UC" and "3B42RT-C") on the same data period. The 3B42RT-Version 6 data were

made available starting 0000 1 October 2008 from the website: ftp://trmmopen.gsfc.nasa.gov/pub/merged/, while the recorded daily precipitation observations of the two study basins have been collected from January 2000 to September 2010. Thus, we selected an overlapping time span of two complete years for verification, from October 2008 to September 2010, as our study period.

3. Results

[9] Our comparison and validation were first performed over three domains, including all selected grid boxes, Grid 0501 (the nested grid containing a maximum of five rain gauges within each basin), and the basin-averaged analysis (hereafter referred to as "basin average"). Thus, the 3B42RT's error characteristics and their changing trends before and after the climatological calibration can be cross-checked over different domains, which increases confidence in the evaluation results.

[10] Plots of daily and monthly comparison of 3B42RT-UC and 3B42RT-C versus gauge observations are shown in Figure 2. For the Laohahe basin, the linear correlation coefficient (hereafter CC) between 3B42RT and observed precipitation gradually decreases from 3B42RT-UC to 3B42RT-C for all three domains (Figures 2a, 2b, 2e, 2f, 2i, and 2j). The daily mean error (mm), bias (%), and root-mean-square error (mm) (ME, BIAS, and RMSE hereafter) of 3B42RT-C are significantly higher than those of 3B42RT-UC. Taking the domain of 16 selected grids (i.e., "16 Grids_L" in Figure 2), for example, the BIAS value increased from 78.73% of 3B42RT-UC (Figure 2a) to 109.91% of 3B42RT-C (Figure 2b). Compared to random error and bias, the changes in the contingency table statistics are not large, but the indices of probability of detection, false alarm rate, and critical success index (POD, FAR, and CSI hereafter) still have a relatively worse performance at the daily time scale after calibration. Similarly, the monthly scatterplots (Figures 2c, 2d, 2g, 2h, 2k, and 2l) show that 3B42RT-UC apparently outperformed 3B42RT-C according to all statistics. This suggests that the CCA failed to reduce the error and enhance the data accuracy of 3B42RT here and perhaps at some other high-latitude regions. In practice, the calibrations for the 40°–50° latitude belts of both hemispheres are taken to be the calibrations that apply just equatorward of 40° [*Huffman et al.*, 2007, 2010]. In other words, the 40°N and S calibration ratios in the current TMPA real-time system are simply extended to all higher latitudes due to the lack of TCI data to serve as the reference. Hence, it is quite plausible that the negative biases in the grid cells of the equatorward 40° resulted in a further increase in the positive bias of 3B42RT-UC in the Laohahe basin after CCA. Our evaluation results confirm that the calibration-processing scheme evidently needs to be improved.

[11] In contrast, the CCA exhibits an effective improvement on 3B42RT in the low-latitude Mishui basin. Both the daily and monthly CC values of 3B42RT-C are higher than those of 3B42RT-UC (Figures 2m–2x). The CCA significantly reduced the ME and BIAS between 3B42RT and gauge observations over all three domains as anticipated by the algorithm developers. Meanwhile, the monthly RMSE of 3B42RT-C also exhibits a better performance than that of the 3B42RT-UC (decreasing by approximately 25% for 11 grids, 35% for Grid 0501, and 40% for basin average, respectively). However, it is worth noting that the daily RMSE of 3B42RT-C did not improve over that of 3B42RT-UC (Figures 2m, 2n, 2q, 2r, 2u, and 2v). The negative bias correction for the Mishui basin seemed to raise the 3B42RT-UC overall, which resulted in amplifying overestimation with large rain events. Since RMSE could be affected sensitively by a small number of large errors, the daily RMSE still increased despite the decreased bias. This result is similar to the larger-scale result reported by *Huffman et al*. [2010]. With respect to the skill of detecting rainy events, the indices of POD and CSI are substantially increased after calibration. But interestingly, we found that the FAR also evidently increased from 3B42RT-UC to 3B42RT-C. The authors argue that such a phenomenon is closely related to the reintroduction of satellite data sources taken by the TMI-TCI and TCI-3B43 calibrators. Among which, the TCI calibrator combines data from both TMI and the PR (TRMM product 2B31) data. As monthly multisatellite products of TRMM level 3, the 3B43 calibrator provides a global 0.25° × 0.25° combination of all currently available TCI, TMI, Special Sensor Microwave Imager (SSMI) and Special Sensor Microwave Imager-Sounder (SSMIS) on Defense Meteorological Satellite Program (DMSP), Advanced Microwave Scanning Radiometer for Earth Observing System (AMSR-E) on Aqua, Advanced Microwave Sounding Unit-B (AMSU-B) on NOAA-15, -16, -17, Microwave Humidity Sounder (MHS) on Europe Operational Meteorological (MetOP) satellite, and geosynchronous earth orbit infrared (geo-IR) Brightness Temperature (Tb) estimates (note: more detailed information on 3B43 data source and processing can be found in the NASA technical document available at ftp://precip.gsfc.nasa.gov/pub/trmmdocs/3B42_3B43_doc.pdf). Therefore, the new calibration imperceptibly boosts the frequency of input data sets in the TMPA real-time system. Computationally, this will result in an increase in the number of rainy events detected by satellite, i.e., item "satellite yes" of the 2 × 2 contingency table (a: satellite yes, observation yes; b: satellite yes, observation no; c: satellite no, observation yes; and d: satellite no, observation no) in *Wilks* [2006]. Thus, the added satellite detections contribute directly to the observed increases in daily POD and FAR values.

[12] By intercomparing these two basins, we find that both 3B42RT-C and 3B42RT-UC estimates in the low-latitude Mishui basin clearly exhibit better CC values and lower BIAS than those of the high-latitude Laohahe basin. This could be attributed to three major reasons.

[13] (1) The geo-IR data with excellent time-space coverage, but poor correlation with precipitation, become a more important data source for producing the merged 3B42RT in high-latitude regions. That is, the scan frequency of infrared (IR) sensors covering Laohahe basin accounts for about 40.97% of total scans, principally because both TMI and conical average are zero (Table 1). In contrast, the IR scan frequency in the Mishui basin has a smaller proportion of only 14.28%, which is even lower than those of several major passive microwave (PMW) sensors. These increased passive microwave inputs, which have a more direct physical connection to the hydrometeor profiles, provide more accurate data sources for 3B42RT estimates in the low-latitude areas.

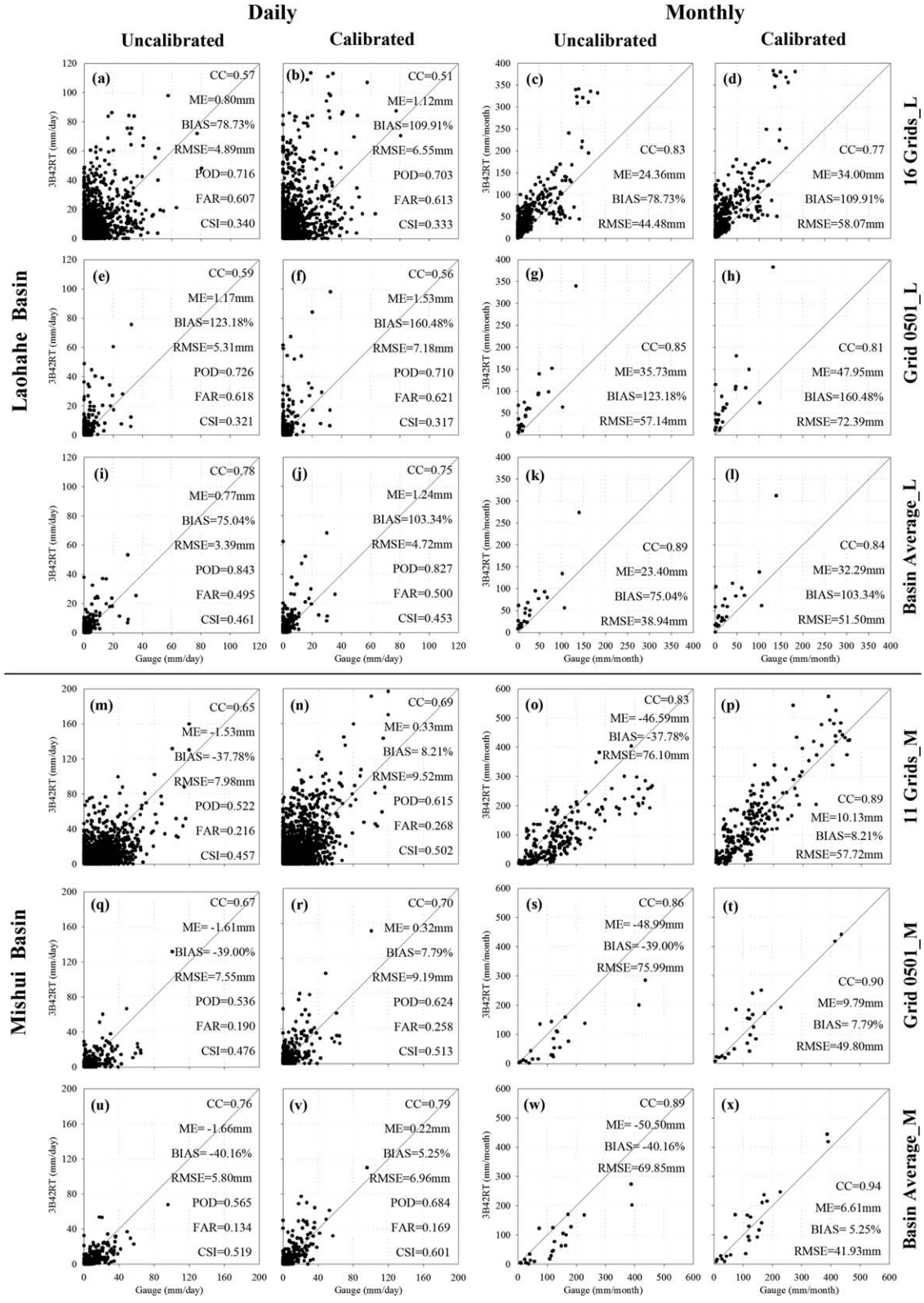

Figure 2. Scatterplots of the (first and third column) uncalibrated and (second and fourth column) calibrated 3B42RT comparison for all selected grids, Grid 0501, and basin average in (top three rows, a–l) the Laohahe basin and (bottom three rows, m–x) the Mishui basin, respectively. The left two columns are the daily 3B42RT versus gauge observation, while the right two columns are the monthly 3B42RT versus gauge observation. Note: The formulae and meaning of all statistical indices in each plot are described in more detail in Table 1 of *Yong et al*. [2010].

Table 1. Scan Counts of Sensors Introduced Into the TMPA Processing for All Grids Over the Laohahe Basin and Mishui Basin[a]

			Scan Counts (Scan Frequency)	
Source Number	Sensor	Platform	Laohahe Basin	Mishui Basin
0	No Observation		353 (1.83%)	80 (0.86%)
1	AMSU	NOAA-15, 16, 17	22,041 (11.45%)	18,192 (19.48%)
2	TMI	TRMM	0	16,852 (18.05%)
3	AMSR	Aqua	24,946 (12.95%)	10,105 (10.82%)
4	SSMI	DMSP-F13, 14	13,656 (7.09%)	5061 (5.42%)
5	SSMIS	DMSP-F16, 17	0	0
6	MHS	MetOP-1	24,252 (12.59%)	14,098 (15.10%)
30	AMSU and MHS average	Refer to Appendix A	28,446 (14.77%)	10,741 (11.50%)
31	Conical average	Refer to Appendix A	0	4910 (5.26%)
50	IR	GEOS, GMS, Meteosat	78,894 (40.97%)	13,337 (14.28%)
1, 2, 3, 4, 5, 6 + 100	Sparse-sample HQ		0	0
Total scan counts for all sensors			192,588	93,376

[a]The scanning approach of microwave sensors and their score formulations: refer to Appendix A. The international constellation of geosynchronous-orbit meteorological satellites including the Geosynchronous Operational Environmental Satellites (GOES, United States), the Geosynchronous Meteorological Satellite (GMS, Japan), and the Meteorological Satellite (Meteosat, European Community) provide the infrared (IR) data on a 4 km-equivalent grid over the latitude band 60° N-S for TMPA system.

[14] (2) The TRMM-based TMI (coverage of 40°N-S) can completely cover the Mishui basin (e.g., the scan frequency of TMI is approximately 18.05% over Mishui basin, see Table 1). Therefore, the first intercalibration to TMI for the PMW data in the TMPA system was performed rather well in this low-latitude basin. Likewise, the TMI-TCI used as the climatological calibrator is also limited within the latitude bands between 40°N and S. Thus, a direct climatological calibration for IR-based estimates is obtained in Mishui basin.

[15] (3) Last, winter snowfall is another important factor that seriously affects the satellite precipitation estimates in higher latitudes, which has been highlighted by *Yong et al.* [2012].

[16] To look further into the error characteristics of the TMPA estimates, we compared the monthly mean precipitation and the monthly variations of statistical indices of daily 3B42RT-C and 3B42RT-UC versus gauge observations for the 16 selected 0.25° grid boxes in the Laohahe basin and the 11 grid boxes in the Mishui basin (Figure 3). Similar to the results in Figure 2, Figures 3a and 3b illustrate systematic overestimation with 3B42RT-UC for the Laohahe basin and underestimation for the Mishui basin at monthly time scale. It is clear that the CCA generally elevates the TMPA estimates so that the 3B42RT-C agrees well with the observed precipitation in the Mishui basin, but making the performance in the Laohahe basin poorer than before. In terms of CC, there is little difference between 3B42RT-UC and 3B42RT-C for these two basins (Figures 3c and 3d). For the Laohahe basin, the largest relative biases occur in winter (Figure 3e). Due to the interference of ice and snow cover over land surfaces to the passive microwave retrievals, the available PMW-based calibrations of IR and the PMW data themselves covering higher-latitude regions cannot offer accurate estimates with snowing events [*Grody*, 1991; *Ferraro et al.*, 1998; *Yong et al.*, 2012]. Thus, both the poorer satellite retrievals and the less actual precipitation during winter months jointly drive the remarkable relative bias shown above. Furthermore, the CCA made this problem more serious for the Laohahe basin (e.g., the BIAS of 3B42RT-UC exceeded 8000% on December 2009, see Figure 3e). In contrast, the average BIAS of Mishui basin during our study period was improved, with a drop from −37.78% before calibration to only 8.21% after calibration. Figures 3g and 3h further confirmed that the monthly climatological calibration cannot effectively reduce RMSE values at the daily scale for either area. Rain probability is nearly the same for 3B42RT-UC and 3B42RT-C in the Laohahe basin (Figure 3i), while in the low-latitude Mishui basin the climatological bias correction exhibits an increase in POD (Figure 3j).

[17] Having seen that both basins exhibit lower CC and POD and larger BIAS in the winter compared to other seasons, we consider that such worse performance in winter comes from two compounding effects.

[18] (1) Some high-frequency channels of PMW sensors (e.g., the 89 and 150 GHz channels of AMSU-B) might detect more scattering associated with the frozen land surface and ice particles in winter, which seriously interferes with the PMW-based retrievals [*Grody*, 1991; *Vila et al.*, 2007]. Thus, the typically more reliable microwave estimates lose their physical connection to surface precipitation during the cold season, especially during snowy days.

[19] (2) The apparent deficiency in detecting precipitation of PMW sensors in winter will further affect the calibration of the TMPA estimates. For the higher-latitude bands (beyond 40°N-S), the microwave estimates are not even available to calibrate the IR data.

[20] To help diagnose the influence of CCA on event-scale precipitation values, we compared the intensity distribution of the daily precipitation amount and the daily precipitation events for 3B42RT-UC and 3B42RT-C estimates with that of the gauge data. For our study, the probability distribution functions (PDFs) are computed over the 16 selected grid boxes in the Laohahe basin and 11 grid boxes in the Mishui basin, as shown in Figure 4. The intensity distribution of daily precipitation amount provides unique insights into the error dependence on rain rate and also the potential impact of the errors on hydrological applications [*Tian et al.*, 2009]. Figures 4a and 4b clearly show that the differences of precipitation amount between 3B42RT-UC and 3B42RT-C are insignificant in lower rainfall intensities for both basins. However, at higher rain rates (i.e., >16 mm/d for the Laohahe and >10 mm/d for the Mishui

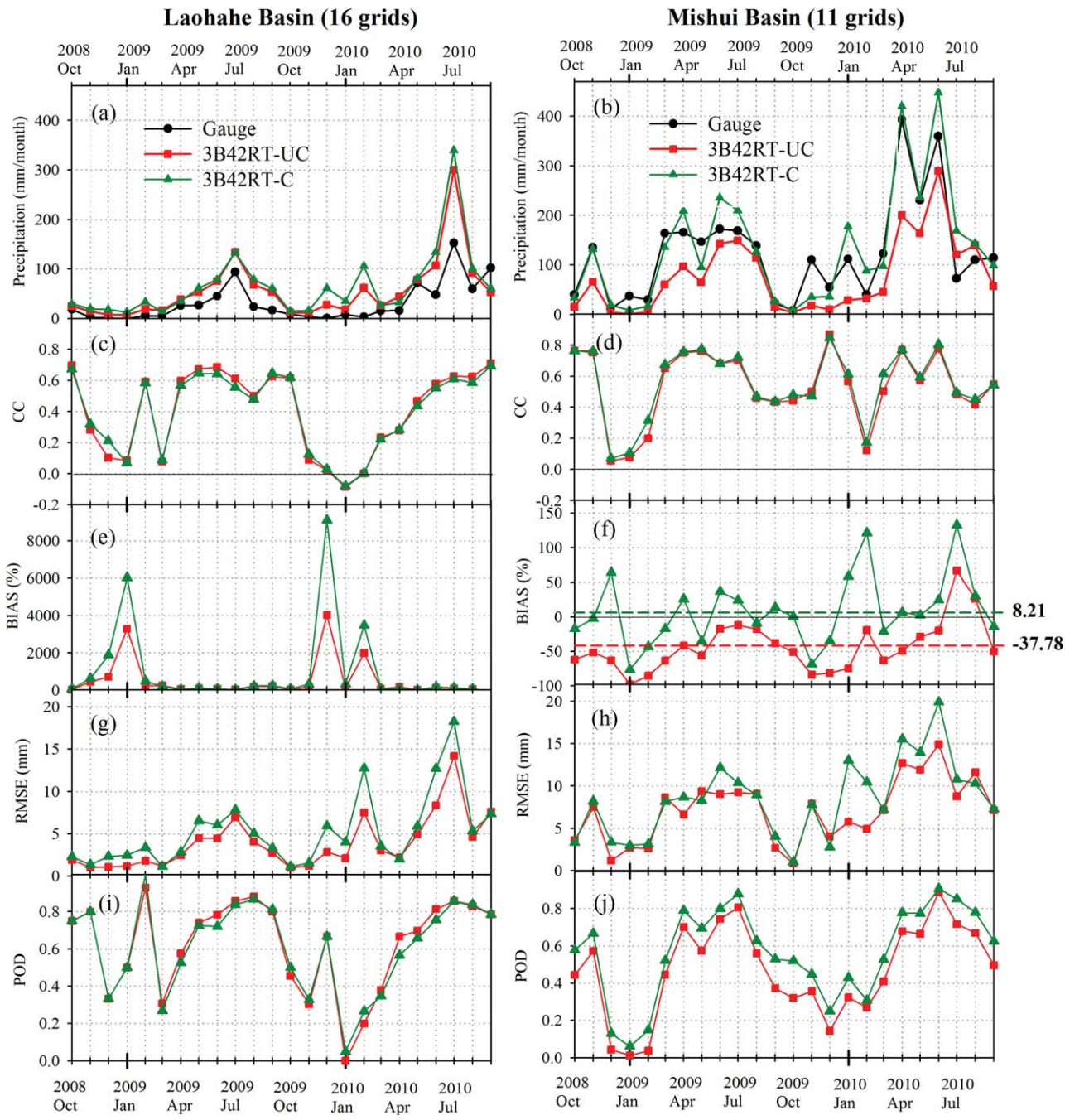

Figure 3. (a and b) Average monthly precipitation time series and (c–j) monthly variations of statistical indices of daily uncalibrated and calibrated 3B42RT versus gauge observation for (left column) the 16 selected grid boxes in the Laohahe basin and (right column) the 11 selected grid boxes in the Mishui basin: (c and d) correlation coefficient, (e and f) relative bias, (g and h) root-mean-square error, and (i and j) probability of detection.

basin), the differences become more significant. This suggests that the CCA tends to affect the BIAS for 3B42RT by primarily impacting the precipitation estimates at higher rain rates. In terms of hydrological applications, this calibration can have a major impact on the 3B42RT-driven simulations or predictions for surface runoff associated with medium-high rain rates, while it has less effect on the antecedent soil moisture related to lower rain rates.

[21] Due to the effect of a stronger East Asian monsoon, the rain rate distribution of observed precipitation in the Laohahe basin exhibits two peak values of approximately 10 and 32 mm/d (Figure 4a). Yet, the distribution over the Mishui basin presents a single-peak pattern (peak value of 32 mm/d, see Figure 4b), which is physically associated with the local Mei-Yu system and its warm season convection [*Yu et al.*, 2007]. Surprisingly, the intensity distribution patterns of 3B42RT-UC and the gauge observations were

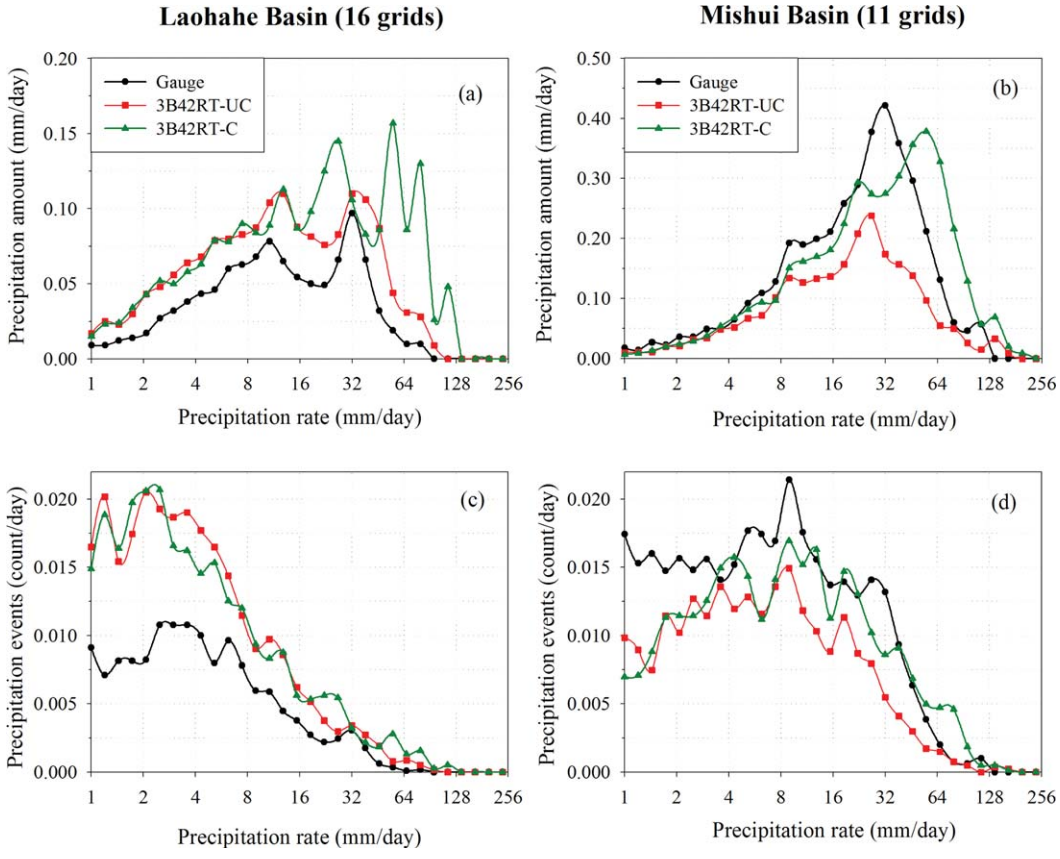

Figure 4. PDFs of daily uncalibrated and calibrated 3B42RT versus gauge observation for (left column) the 16 selected grid boxes in the Laohahe basin and (right column) the 11 selected grid boxes in the Mishui basin: (a and b) daily precipitation amount (mm/d), and (c and d) precipitation events (count/d) as a function of precipitation rate (mm/d), respectively. The logarithmic scale was used to bin the precipitation rates.

found to be quite similar for both validation basins, while 3B42RT-C demonstrated significant discrepancies, particularly at higher rain rates. Furthermore, it is the overestimation at higher rain rates that increases the dynamic range of daily rainfall after the CCA calibration. Statistically, the effect of the dynamic change of high-intensity rainfall on the RMSE value is evidently greater than that of lower rain rates. Therefore, the daily RMSE of 3B42RT for both basins increased when the monthly CCA calibration was applied (as shown in Figures 3g and 3h). In the Mishui basin, the overestimation at higher rain rates (>60 mm/d) has a stronger impact on the variation amplitude of daily 3B42RT-C relative to the underestimation at lower rain rates (Figure 4b). Thus, the daily RMSE for 11 selected grids worsened from 7.98 mm of 3B42RT-UC to 9.52 mm of 3B42RT-C (see Figures 2m and 2n), though the monthly CCA substantially reduced the BIAS over this basin. Consequently, users should consider whether this behavior is undesirable for their applications, especially for applications that are sensitive to higher rain rates such as floods and landslides.

[22] On the other hand, the intensity distributions of the daily number of precipitation events can better reveal the errors at low rain rates (Figures 4c and 4d). For the Laohahe basin, both 3B42RT-UC and 3B42RT-C overestimate approximately 20%–180% of the events across the range of 1–32 mm/d (Figure 4c). Although these two satellite-based data sets have similar patterns in their PDFs of precipitation events, 3B42RT-C yields more events than 3B42RT-UC for higher rain rates between 16 and 128 mm/d. In comparison, these two precipitation estimates underestimate about 5%–60% events in the range of 1–4 mm/d over the Mishui basin. Moreover, the 3B42RT-C evidently captures more rainy events than 3B42RT-UC in the range of 10–100 mm/d despite that they have better agreement at low rain rates. This further supports our aforementioned explanation for the increase of daily POD and FAR values after the CCA calibration in the Mishui basin.

[23] Additionally, scatterplots in Figure 4 illustrate an interesting error feature in that the 3B42RT-UC systematically overestimated gauge observations in the Laohahe basin, while an opposite underestimation occurred in the Mishui basin. The CCA seems to substantially elevate the 3B42RT estimates over both validation sites, thereby effectively reducing the underestimated bias of Mishui basin but further worsening the overestimation of Laohahe basin. Spatially, a much broader view will be helpful to analyze and understand the transferability of these error characteristics from the local study basins to the globe.

[24] Figures 5a–5e show the global maps of mean daily precipitation difference before and after application of the CCA (i.e., 3B42RT-C – 3B42RT-UC) for the whole study

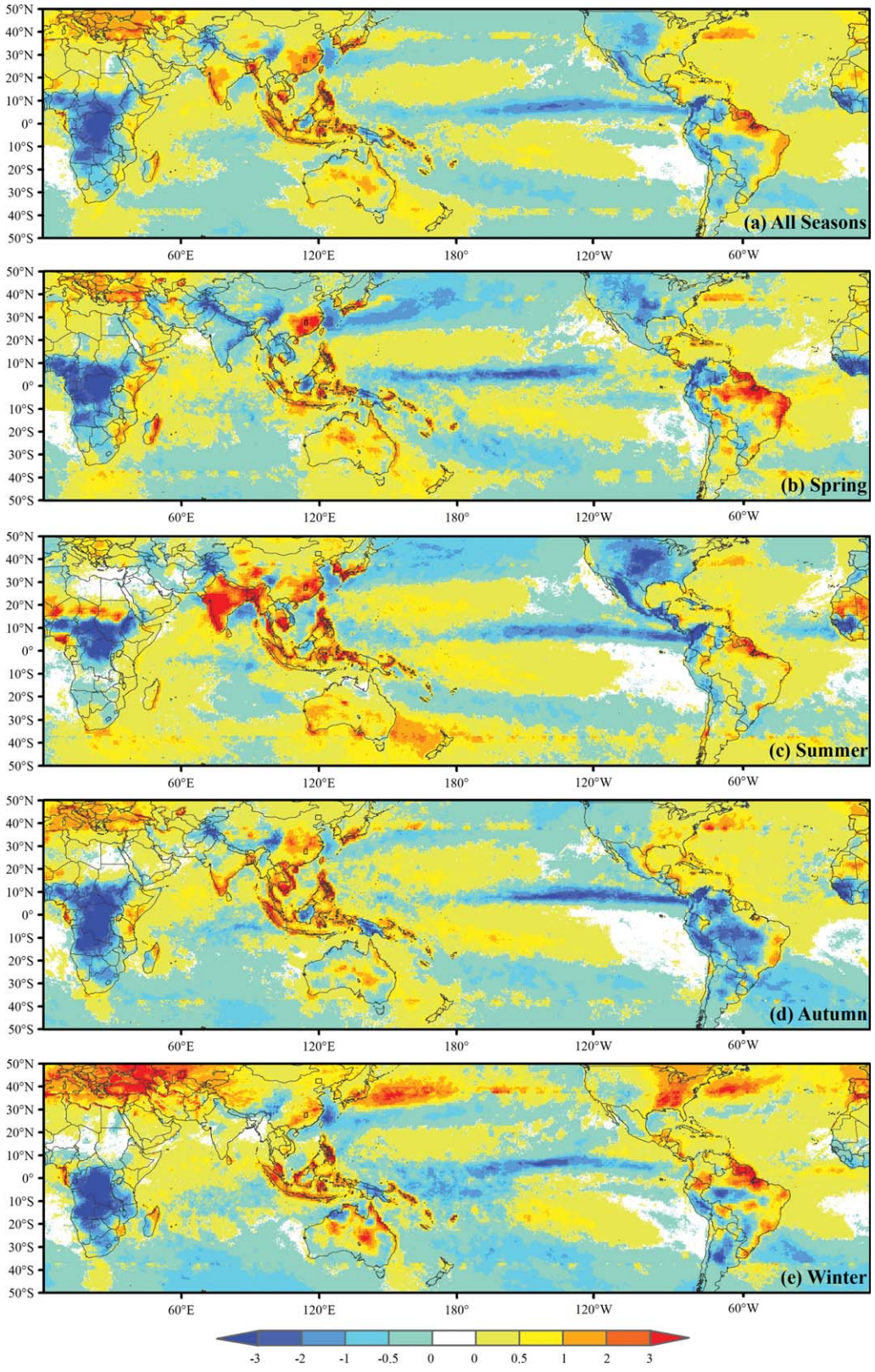

Figure 5. Global map of the mean daily precipitation difference between uncalibrated and calibrated 3B42RT data sets (3B42RT-C – 3B42RT-UC, mm/d) for (a) all seasons, (b) spring (March-May), (c) summer (June-August), (d) autumn (September-November), and (e) winter (December–February).

period and for each season. First, one can see that the CCA raised the 3B42RT estimates over most regions of China, especially for the southeastern portions with a significant increase (Figure 5a). Moreover, the differences between 3B42RT-UC and 3B42RT-C exhibit rather strong seasonal dependencies. In terms of southeastern China covering the Mishui basin, the larger relative biases primarily occurred in the spring and summer seasons (Figures 5b and 5c). We compared our results with those of *Shen et al*. [2010] who used hourly gauge analyses including ~2000 CMA stations over the contiguous China to examine the performance of six current mainstream satellite products. Their results indicated that 3B42RT substantially underestimates the Mei-Yu-related precipitation over southern and southeastern China. The upward adjustments of the CCA calibration effectively reduced such systematic underestimation over this region, particularly in warm seasons. On the other hand, Figure 5 also illustrates that the contribution of 3B42RT-C's overestimation for northeastern China mainly came from the summer and winter seasons. This result supports the conclusion of *Yong et al*. [2012] that the larger bias and error of 3B42RT over the Laohahe basin are chiefly attributed to the unrealistic overestimation for the summer rainstorms and the winter snowfall. Apparently, the simplified smooth-fill scheme in the CCA for the 40°–50° latitude belts increased the 3B42RT-UC estimates and consequently worsened their performance with high rain rates over this high-latitude basin. Generally speaking, the seasonal variations of precipitation over both validation basins are consistent with our observations and explanations in Figure 3.

[25] The global maps displayed in Figure 5 also give an overall depiction of how the calibration scheme works over both land and ocean. Since the gauge-adjusted influence in CCA is only at work over land areas, one tends to see relatively larger differences between 3B42RT-UC and 3B42RT-C over the land areas than over the ocean. Most notably along the western coast of India, but also in Europe, Myanmar, Cambodia, Indonesia and Philippine Islands, southern Japan, and northeastern South America, the CCA calibration significantly elevated the 3B42RT estimates as well as in southeastern China. Meanwhile, significant reductions resulted following the CCA calibration in central Africa, midwestern United States, Latin America, and western coastal South America. Almost all the regional changes show strong seasonal dependencies. For example, Europe exhibits much higher differences in winter than the other three seasons due to the more erroneous retrievals with snow events during the cold season. Over India, the 3B42RT overestimated rainfall during premonsoon period (March, April, and May) and significantly underestimated during the monsoon period (June, July, August, and September), which have been documented in previous studies [e.g., *Islam and Uyeda*, 2006]. Figures 5b and 5c show that the CCA tends to reduce 3B42RT's overestimation in spring and increased the underestimated monsoon-related precipitation in summer. Likewise, over the midwestern United States 3B42RT dramatically overestimated the strong convective events in summer, as seen from existing studies with ground-based validation data [e.g., *Tian et al*., 2009; *Gourley et al*., 2010]. Figure 5c shows that such overestimation during the summer months was also reduced by the CCA calibration. Due to the lack of accurate ground observations, the current study does not quantify the systematic errors of 3B42RT against surface validation data across the globe. But we believe that from the global perspective the systematic errors in TMPA were generally alleviated over land when the CCA was applied, as discussed by *Huffman et al*. [2010].

4. Conclusions and Recommendations

[26] As one of the most important upgrades during the evolution of the TMPA real-time system, the CCA was regarded as an operational approach that can introduce climatological gauge information to effectively reduce the systematic errors (similar to the research-quality 3B42V6), while maintaining the near-real-time availability of 3B42RT itself. In this study, we compared and validated this upgrade over two representative basins of China situated at high- and low-latitude bands, respectively, by using local independent rain gauge networks.

[27] Our analyses indicate that the CCA generally provides improved rainfall estimates for the low-latitude Mishui basin, while poorer performances are obtained after the calibration for the high-latitude Laohahe basin, primarily in winter. This result demonstrates that the simplified calibration scheme in the current TMPA system of directly applying the calibrations along the 40° latitude to the latitude belts between 40° and 50° is really not an effective method for high-latitude precipitation estimates. It is likely that this problem will be resolved when GPM goes into operation because the GPM Microwave Imager and the dual-frequency PR will cover 65°N-S, providing the necessary calibrators for higher latitudes. But currently, the TMPA users should note that they might get worse performance when selecting the calibrated 3B42RT data sets in regions beyond 40°N-S than using the 3B42RT-UC precipitation.

[28] Overall, our evaluation shows that the 3B42RT-UC estimates tend to overestimate precipitation over the high-latitude Laohahe basin (especially in winter) and underestimate over the low-latitude Mishui basin. This finding is consistent with the assessment results of *Shen et al*. [2010]. The CCA seems to elevate the 3B42RT estimates over these two sites so as to reduce the random error and bias for the Mishui basin but unfavorably increased the overestimation for Laohahe basin.

[29] Compared to other seasons, the systematic error was notably higher during the winter in the Laohahe basin. This arises because at high latitudes the frozen surfaces prevent retrievals with passive microwave window channels that respond to scattering. In addition, our assessment illustrates that the CCA worked rather well for the low-latitude Mishui basin, having effectively reduced the error and bias of original 3B42RT and improved its skill of detecting rainy events. But we note that the daily RMSE became worse after the calibration. This is because the monthly climatological calibrators in the CCA increase the dynamic range of daily precipitation with higher rain rates. Moreover, we found that the CCA changed the intensity distribution pattern of middle and high rain rates for both of the basins. In other words, the CCA improves on the long-term estimates of total precipitation amounts, at the price of altering the distribution features of rain rates. By comparing with the

3B42RT-C, the 3B42RT-UC estimates exhibit better distributions of rainfall intensity, as compared to independent rain gauges. Therefore, it seems important to continue providing the uncalibrated combined precipitation as an additional field in new versions of 3B42RT, as is being done in Version 7. Such additional information allows the TMPA users to employ local high-resolution (e.g., daily or subdaily) real-time surface precipitation observations in combination with the uncalibrated 3B42RT to create new precipitation products appropriate to the user's local application.

[30] Finally, our analysis was simply extended to the global scale to examine the differences between 3B42RT-C and 3B42RT-UC from a broader perspective. The most obvious differences at the global scale are the strong seasonal dependence. Moreover, the global analysis implies that the systematic errors in TMPA were generally alleviated over land after the CCA calibration. However, we note that the use of the climatological gauge data in the CCA calibrators cannot adjust for the varying rainstorm characteristics during various years. Therefore, the current CCA improvement is primarily in the sense of simply reducing the error and bias over the globe, rather than completely and fully correcting the error structures and pattern features of satellite precipitation data for local areas.

[31] Although the ground-based validation in this study is limited to two middle-sized basins at different latitudes, we considered that other regions in the globe might experience similar issues as well [*Huffman et al.*, 2010]. We expect that the assessment reported in this paper will provide a better understanding of the improvements and potential limitations of this CCA upgrade. Looking into the forthcoming GPM era, we strongly believe that further efforts for examining those crucial upgraded algorithms will substantially benefit the retrieval algorithms to produce more reliable and accurate satellite precipitation estimates for users of the Earth science community.

Appendix A: Scanning Approaches of Microwave Sensors Introduced Into the TMPA System and Score Formulations of Their Scan Counts

[32] In terms of scanning approach, the microwave sensor sources of 3B42RT can be separated into two types, i.e., cross-tracking scanning including AMSU and MHS, and conical scanning with TMI, AMSR, SSMI, and SSMIS. The averages (30 and 31) provide the average values of all the pertinent microwave data (sounder or conically scanning) when more than one satellite overpass of that type occurs in the 3 h period. Four data files of 3B42RT (i.e., on the time of 0900 UTC 7 July 2009, 1200 UTC 18 August 2009, 2100 UTC 3 May 2010, and 1500 UTC 29 May 2010) were missed by the TMPA system. Therefore, 5836 data files of 3B42RT were used in this study during the period of October 2008 to September 2010. The calculating method of scan counts can be expressed as follows: (1) there are 33 TMPA grid boxes ($0.25^\circ \times 0.25^\circ$) covering the Laohahe basin, so its corresponding total scan counts are 33 grids $\times$ 5836 files = 192,588 counts; (2) similarly, the total scan counts for Mishui basin are 16 grids $\times$ 5836 files = 93,376 counts; and (3) the scan frequency of a certain sensor source (SF_i) can be calculated as

$$SF_i = \frac{SC_i}{SC_{total}} \times 100\%, \tag{A1}$$

where SC_i is the scan counts of one sensor, and SC_{total} is the total scan counts for all sensors.

[33] **Acknowledgments.** The TMPA data used in this study were provided by the NASA/Goddard Space Flight Center's Laboratory for Atmospheres and PPS, which develop and compute the TMPA as a contribution to TRMM. The authors thank three anonymous reviewers who helped to improve the earlier version of this paper. This work was financially supported by the Major Program of National Natural Science Foundation of China (51190090) and the 111 Project (B08048). Also, this work is partially sponsored by Natural Science Foundation of Jiangsu Province (BK2012813), Open Research Fund of Key Laboratory of Digital Earth, Center for Earth Observation and Digital Earth, Chinese Academy of Sciences (2011LDE008), Special Basic Research Fund for Methodology in Hydrology (2011IM011000), Qinglan Project of Jiangsu Province, and Open Fund of State Key Laboratory of Hydrology-Water Resources and Hydraulic Engineering (2012490111).

References

Adler, R. F., et al. (2003), The version 2 Global Precipitation Climatology Project (GPCP) monthly precipitation analysis (1979–present), *J. Hydrometeorol.*, *4*(6), 1147–1167.

Chokngamwong, R., and L. Chiu (2008), Thailand daily rainfall and comparison with TRMM products, *J. Hydrometeorol.*, *9*, 256–266.

Ferraro, R. R., E. A. Smith, W. Berg, and G. J. Huffman (1998), A screening methodology for passive microwave precipitation retrieval algorithms, *J. Atmos. Sci.*, *55*, 1583–1600.

Grody, N. C. (1991), Classification of snow cover and precipitation using the special sensor microwave imager, *J. Geophys. Res.*, *96*(D4), 7423–7435.

Gourley, J. J., Y. Hong, Z. L. Flamig, L. Li, and J. H. Wang (2010), Intercomparison of rainfall estimates from radar, satellite, gauge, and combinations for a season of record rainfall. *J. Hydrometeorol.*, *49*, 437–452.

Hong, Y., R. F. Adler, and G. J. Huffman (2007), An experimental global prediction system for rainfall-triggered landslides using satellite remote sensing and geospatial datasets, *IEEE Trans. Geosci. Remote Sens.*, *45*(6), 1671–1680.

Hossain, F., and D. P. Lettenmaier (2006), Flood prediction in the future: Recognizing hydrologic issues in anticipation of the Global Precipitation Measurement mission, *Water Resour. Res.*, *42*, W11301, doi:10.1029/2006WR005202.

Huffman, G. J, R. F. Adler, D. T. Bolvin, G. Gu, E. J. Nelkin, K. P. Bowman, Y. Hong, E. F. Stocker, and D. B. Wolff (2007), The TRMM Multisatellite Precipitation Analysis (TMPA): Quasi-Global, multi-year, combined-sensor precipitation estimates at fine scales, *J. Hydrometeorol.*, *8*, 38–55.

Huffman, G. J, R. F. Adler, D. T. Bolvin, and E. J. Nelkin (2010), The TRMM Multi-satellite Precipitation Analysis (TMPA), in *Satellite Applications for Surface Hydrology*, edited by F. Hossain and M. Gebremichael, pp. 3–22, Springer, New York.

Islam, M. N., and H. Uyeda (2006), TRMM observed vertical structure and diurnal variation of precipitation in South Asia, paper presented at the IEEE International Geoscience and Remote Sensing Symposium (IGARSS06), *Denver, Colo.*, doi:10.1109/IGARSS.2006.334.

Jiang, S.-H, L.-L Ren, Y. Hong, B. Yong, X.-L Yang, F. Yuan, and M.-W. Ma (2012), Comprehensive evaluation of multi-satellite precipitation products with a dense rain gauge network and optimally merging their simulated hydrological flows using the Bayesian model averaging method. *J. Hydrol.*, 452–453, 213–225, doi:10.1016/j.jhydrol.2012.05.055.

Kidd, C. and G. J. Huffman (2011), Global precipitation measurement, *Meteorol. Appl.*, *18*(3), 334–353.

Liang, J. Z., and Z. Y. Liu (2010), *Research on Medium- and Small-Size Rivers of Monitoring and Early Warning Prediction [in Chinese]*, Science Press, Beijing.

Rudolf, B., H. Hauschild, W. Rueth, and U. Schneider (1994), Terrestrial precipitation analysis: Operational method and required density of point measurements, in *Global Precipitation and Climate Change, NATO ASI Ser.* I, vol. *26*, edited by M. Desbois and F. Desalmond, pp. 173–186, Springer-Verlag Berlin Heidelberg.

Shen, Y., A. Xiong, Y. Wang, and P. Xie (2010), Performance of high-resolution satellite precipitation products over China, *J. Geophys. Res.*, *115*, D02114, doi:10.1029/2009JD012097.

Su, F., H. Gao, G. J. Huffman, and D. P. Lettenmaier (2011), Potential utility of the real-time TMPA-RT precipitation estimates in streamflow prediction, *J. Hydrometeorol.*, *12*, 444–455.

Tapiador, F. J., et al. (2012), Global precipitation measurement: Methods, *datasets and applications. Atmos. Res.*, 104–105, 70–97, doi:10.1016/j.atmosres.2011.10.021.

Tian, Y., C. D. Peters-Lidard, B. J. Choudhury, and M. Garcia (2007), Multitemporal analysis of TRMM-based satellite precipitation products for land data assimilation applications, *J. Hydrometeorol.*, *8*, 1165–1183.

Tian, Y., C. D. Peters-Lidard, J. B. Eylander, R. J. Joyce, G. J. Huffman, R. F. Adler, K. Hsu, F. J. Turk, M. Garcia, and J. Zeng (2009), Component analysis of errors in satellite-based precipitation estimates, *J. Geophys. Res.*, *114*, D24101, doi:10.1029/2009JD011949.

Vila, D., R. Ferraro, and R. Joyce (2007), Evaluation and improvement of AMSU precipitation retrievals, *J. Geophys. Res.*, *112*, D20119, doi:10.1029/2007JD008617.

Wilks, D. S. (2006), *Statistical Methods in the Atmospheric Sciences*, Elsevier, New York.

Xie, P., and P. A. Arkin (1996), Analysis of global monthly precipitation using gauge observations, satellite estimates, and numerical model predictions, *J. Clim.*, *9*, 840–858.

Yong, B., L.-L. Ren, Y. Hong, J.-H. Wang, J. J. Gourley, S.-H. Jiang, X. Chen, and W. Wang (2010), Hydrologic evaluation of Multisatellite Precipitation Analysis standard precipitation products in basins beyond its inclined latitude band: A case study in Laohahe basin, China, *Water Resour. Res.*, *46*, W07542, doi:10.1029/2009WR008965.

Yong, B., Y. Hong, L.-L. Ren, J. J. Gourley, G. J. Huffman, X. Chen, W. Wang, and S. I. Khan (2012), Assessment of evolving TRMM-based multisatellite real-time precipitation estimation methods and their impacts on hydrologic prediction in a high latitude basin, *J. Geophys. Res.*, *117*, D09108, doi:10.1029/2011JD017069.

Yong, B., L.-L. Ren, Y. Hong, J. J. Gourley, X. Chen, J.-W. Dong, W.-G. Wang, Y. Shen, and J. Hardy (2013), Spatial-temporal changes of water resources in a typical semi-arid basin of North China over the past 50 years and assessment of possible natural and socioeconomic causes, *J. Hydrometeorol.*, doi:10.1175/JHM-D-12–0116.1, in press. http://journals.ametsoc.org/doi/abs/10.1175/JHM-D-12-0116.1.

Yu, R., Y. Xu, T. Zhou, and J. Li (2007), Relation between rainfall duration and diurnal cycle in the warm season precipitation over central eastern China, *Geophys. Res. Lett.*, *34*, L13703, doi:10.1029/2007GL030315.